crystals

MDPI

Article

The Effect of the Distance between Ultrasonic Horn and Torch on the Microstructure of Ultrasonic-Assisted Gas Tungsten Arc Welded Inconel 690 Alloy Joint

Yunhao Xia [1,2], Xiaoyu Cai [1], Bolun Dong [1,*] and Sanbao Lin [1,*]

1 State Key Laboratory of Advanced Welding and Joining, Harbin Institute of Technology, Harbin 150001, China; xyharch@163.com (Y.X.); xycai@hit.edu.cn (X.C.)
2 Zhengzhou Research Institute, Harbin Institute of Technology, Zhengzhou 450000, China
* Correspondence: bldong@hit.edu.cn (B.D.); sblin@hit.edu.cn (S.L.)

Abstract: The study focuses on investigating the relationship between the ultrasonic effect and microstructure of ultrasonic-assisted gas tungsten arc welding (UA-GTAW) Inconel690 alloy joints. The influence of ultrasonic vibrations on Inconel690 plates was examined, while also clarifying the distribution pattern of the ultrasonic effect across the plate. Furthermore, actual welding experiments were performed by varying the distance between the ultrasonic horn and the welding torch. The results revealed that there were changes in both grain growth direction within the weld zone and refinement effects achieved under different distances. The optimal refinement of primary and secondary dendrite arm spacing was observed at distances of 60 mm and 180 mm between the welding torch and ultrasonic horn. The hardness of weld zone reached 235HV$_1$ when the distance between ultrasonic horn and welding torch is 180 mm.

Keywords: ultrasonic; inconel690 alloy; microstructure

Citation: Xia, Y.; Cai, X.; Dong, B.; Lin, S. The Effect of the Distance between Ultrasonic Horn and Torch on the Microstructure of Ultrasonic-Assisted Gas Tungsten Arc Welded Inconel 690 Alloy Joint. *Crystals* **2023**, *13*, 1671. https://doi.org/10.3390/cryst13121671

Academic Editor: Marek Sroka

Received: 16 November 2023
Revised: 5 December 2023
Accepted: 8 December 2023
Published: 10 December 2023

1. Introduction

Nickel-based alloys are widely used in the construction of pressurized water reactors (PWRs), fast neutron reactors (FBRs), and fusion reactors [1,2]. The Inconel690 alloy is a common choice for manufacturing critical structural components in nuclear reactors, such as the reactor pressure vessel (RPV), steam generator tubes (SG tubes), nozzle safety ends, and tube seat penetrations [3]. However, the operational environment of welded joints involving Inconel690 alloy often exposes them to substantial saturated steam and high concentrations of corrosive media, creating conditions conducive to stress corrosion and potential cracking in SG tubes [4,5]. Consequently, these welded joints are identified as structural material weaknesses within nuclear reactors. With the International Atomic Energy Agency and other stakeholders advocating for the extension of expected lifetimes and licenses for prolonged operation of existing nuclear reactors, addressing the microstructural challenges in nickel-based alloy welded joints becomes a critical imperative. Improving the microstructure not only extends the service time of the welded joints but also contributes to the overall structural integrity of the construction, thereby playing a pivotal role in extending the service life of nuclear reactors.

While gas tungsten arc welding is widely used in nuclear reactor structural material welding, owing to its merit of minimal splash, simple operation, and beautiful welding gap, its application to nickel-based alloys presents distinct challenges. However, nickel-based alloys exhibit high convective viscosity and poor flowability, posing challenges in achieving deep penetration during welding [6]. The inherent high convective viscosity and poor flowability of nickel-based alloys hinder the achievement of deep penetration during welding. It is usually necessary to improve flow performance by increasing the welding current. However, the low thermal conductivity of nickel-based alloys causes elevated temperatures within the weld zone, leading to the formation of coarse solidification grains. The presence of coarser grains promotes straight grain boundaries, facilitating the expansion of ductility-dip cracks (DDC). Ultimately, under stress concentration conditions, the welded joint is prone to failure, posing difficulties in meeting the stringent requirements of nuclear reactor lifetimes. Consequently, refining the grain size of the of nickel-based alloys weld zone is crucial for enhancing the service life.

Scholars have effectively enhanced the microstructure of welded joints by adjusting heat input and innovating welding processes. Yan et al. proposed a polarity-switching self-adaptive shunt (PSSAS) method, which makes the tungsten electrode the end of the arc burning and the welding wire and substrate, alternately, the other end of the arc burning [7]. This method decouples the mass transfer thermal force to reduce the heat input to the base metal during the arc melting metals. Zhu et al. utilized the laser hybrid cold metal transfer welding method, demonstrating its efficacy in reducing heat input and improving microstructure and mechanical properties [8]. Zhang et al. altered the shielding gas used in CMT welding to N_2, resulting in an increase in the toughness of the duplex stainless steel weld joint [9].

In addition, numerous studies claim the ultrasonic field can refine the grain size and improve the mechanical properties of welded joints. Ultrasonic-assisted arc welding include the application of ultrasonic-vibration-assisted arc welding and ultrasonic frequency pulse arc welding [10–12]. In welding processes, the introduction of ultrasonic energy into the molten pool generates cavitation and acoustic streaming effects, which influence the molten pool dynamics and alter solidification conditions such as supercooling degree. Consequently, these modifications lead to improvements in the solidification microstructure of weld zones. Aoki et al. utilized numerical simulation to guide ultrasonic-assisted welding, reducing both microstructure refinement and residual stress in welded joints [13]. Watanabe et al. introduced ultrasonic vibrations into the molten pool of ferritic stainless steel and found that when the welding speed was fast, the effect of ultrasonic vibrations on grain refinement was significant [14]. Fattahi et al. added ZrO_2/TiO_2 particles to GTAW welds and used ultrasonic vibrations to make their distribution more uniform, ultimately obtaining fully nanosized fine-grained welds, further demonstrating the influence of ultrasonic vibrations on melt pool flow [15]. Tian and Koli et al. also successfully achieved the refinement of weld microstructure using ultrasonic-assisted CMT [16,17]. Wang et al. used the GTA welding method under ultrasonic excitation to weld Inconel718 and Inconel738 alloys [18,19]. The results of Inconel718 show that compared to regular arc welding, ultrasonic arc promotes uniform element distribution, improves the distribution of the Laves phase in Inconel718 alloy welded joints, destroys its regular network distribution, reduces the size of the Laves phase, and makes it more dispersed. Therefore, the ultrasonic-assisted gas tungsten arc welding (UA-GTAW) is suitable for the nickel-based alloy weld zone refinement challenge and enhancing the service life of welded joints [20].

When ultrasonic vibration propagates in a solid plate, it will be reflected when it meets the boundary of the medium. The incident wave and the reflected wave will be superimposed and interfered inside the plate, thus forming a standing wave [21]. The amplitude and the acoustic pressure will change with the change of position, and there will be maximum and minimum values. Therefore, for plates of different shapes and sizes with the different medium boundary, when they are subjected to ultrasonic vibration, their ultrasonic field distribution is different [22]. However, in current ultrasonic-vibration-assisted welding, scholars neglect the superposition and interference of the ultrasonic field distribution and directly fix the ultrasonic at a certain position or fix the distance between the ultrasonic horn and the welding torch as a fixed value (or the closest position to the welding torch) [23]. In addition, when ultrasonic vibration propagates in solid metal plates, it will experience varying degrees of attenuation due to the different composition of the alloy, and diffraction will occur due to the hard points (some second phase) in the plate. Therefore, the ultrasonic field distribution of metal plates with the same dimensions but different components is also different [24]. Unfortunately, current scholars do not seem to analyze the ultrasonic distribution of different materials. Specifically, there is still a lack of research on the distribution of the ultrasonic field and the influence of the ultrasonic field at different positions on the weld microstructure during the ultrasonic-assisted welding of Inconel690 alloy.

Therefore, this study aims to determine the optimal positioning of ultrasonic assistance during Inconel690 GTAW processing. The acoustic pressure and ultrasonic amplitude were measured and simulated at various positions within the Inconel690 plate upon introducing the ultrasonic field. Subsequently, several key points with significant ultrasonic amplitudes were selected. The distances between these points and the ultrasonic horn were measured, serving as reference for the distance between the ultrasonic horn and welding torch. These determined distances were then utilized in practical welding experiments. Microstructural observations of weld zone samples were conducted to quantify dendrite refinement to ultimately determine the optimal position of the ultrasonic horn. This systematic approach not only enhances the understanding of ultrasonic propagation characteristics on Inconel690 plates but also provides a practical and universally applicable method for optimizing ultrasonic-assisted welding across different alloys.

2. Experimental Apparatus, Materials, and Methods

2.1. Apparatus and Materials

The UA-GTAW system includes a HC HX-800 ultrasonic horn (Jiazhen Ultrasonic Technology, Hangzhou, China), an ultrasonic power supply(Jiazhen Ultrasonic Technology, Hangzhou, China), a REHM tiger 230 AC ultra welding power supply(REHM Welding Technology, Uhingen, Germany), a GTA torch, a 3-axis welding workbench, and a control system. The devices are shown in Figure 1. A single scanning laser vibrometer was employed to measure the amplitude of different position of the plate.

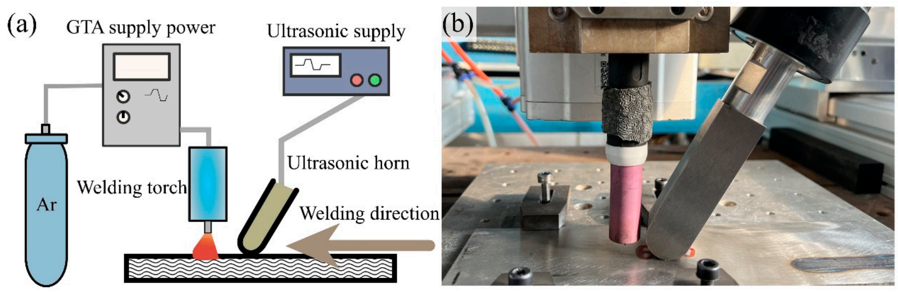

Figure 1. The UA-GTA system: (**a**) the schematic of the system; (**b**) the welding torch and ultrasonic horn.

When ultrasonic waves are transmitted to the base metal through the ultrasonic horn, when there is no relative motion between the ultrasonic horn and the welding torch, the ultrasonic waves will form a more stable ultrasonic field in the welded plate. Therefore, this study aims to establish a fixed relationship between the welding gun and the ultrasonic horn. To facilitate the relative movement between the ultrasonic horn and the welded plate, the contact end between the ultrasonic horn and the metal plate is designed as a circular arc. The ultrasonic output amplitude on the circular arc surface is consistent, and the circular arc segment contacts the workpiece to conduct ultrasonic waves. When the ultrasonic horn is applied to the welded plate, to ensure good contact with the metal plate, a certain pressure is applied to the surface of the workpiece through the pressure adjustment fixture. The ultrasonic horn is positioned radially perpendicular to the welded plate and moving synchronously with the GTA torch during welding. Additionally, it is possible to adjust the distance between the ultrasonic horn and GTA torch.

The substrates used were Inconel690 alloy plates with dimensions of 250 mm in length, 150 mm in width, and 10 mm in height. Table 1 provides the compositions of plates. Pure argon (99.9%) was employed as a shielding gas. Thoriated tungsten cathode was utilized as the tungsten electrode.

Table 1. Chemical compositions of the Inconel690 plates (mass fraction%).

	Ni	Cr	Fe	Mn	C	Cu	Si
Base metal	Balance	28.1	7.86	0.26	0.002	0.19	0.36

2.2. UA-GTAW Process

First, polish the nickel-based alloy plate to a bright finish, clean it with acetone, dry it, and then fix it with a suitable welding fixture. Adjust the mutual position between the welding torch and the plate to be welded through the 3-axis welding workbench so that the welding torch is located at the starting position of the weld bead. Set the motion path of the 3-axis welding workbench according to the length of the weld seam. Fix the distance between the ultrasonic horn and the welding torch. Set welding power supply and ultrasonic power supply parameters.

The welding process Involved the direct current electrode positive, an arc current of 150 A and a welding speed of 100 mm/min. The frequency of ultrasonic vibration is 35 kHz. The ultrasonic power is 800 W. The flow rate of shield gas is 15 L/min.

Turn on the shield gas valve and control the ultrasonic power supply to apply the ultrasonic vibration to the plate. Control the welding power supply to start the arc of the welding torch. At the same time, the 3-axis welding workbench will begin to move according to the predetermined trajectory and began welding. After the platform reaches the predetermined endpoint, welding is complete, and the welding power supply, ultrasonic power supply, and shield gas are turned off. Remove the welded plate to complete the welding. During the welding process, the relative position of the welding equipment is with the welding torch above the plate to be welded. The ultrasonic horn is connected to the torch, located behind the movement of the torch and above the welded plate.

2.3. Microstructure Characteristics and Hardness Test

Following the completion of plate welding, longitudinal/sectional welded joint samples were obtained via wire-cut electrical discharge machining. These samples were subsequently mechanically ground and polished to achieve a smooth surface. The electrolytic etching is performed by using 15 g of Cr_2O_3 and 100 mL of H_2O under a direct current of 10 V for 15 s. The microstructure of the welded joint was observed using a Keyence VHX-1000E optical microscope, while ImageJ software was employed for measuring microstructural dimensions. Ten metallographic images were capture for each weld sample, imported into ImageJ software, and ten positions were select from each image to measure the dendrite arm spacings. The resulting average value represents the mean dendrite arm spacing across different samples. The hardness of the weld zone was evaluated using an HVS-1000A sclerometer. Each sample underwent hardness testing at 10 points, applying a load of 1 kg for a holding time of 15 s.

3. Results and Discussion

3.1. The Distribution Characteristics of Ultrasonic Field

The acoustic impedance of the base metal differs from that of the ultrasonic horn, leading to reflection and transmission of vibrations at the interface when the ultrasonic vibration travel to the base metal. Furthermore, the physical property characteristics and geometric dimensions of the base material can also impact the ultrasonic travel within the base metal. The propagation of ultrasonic waves varies across different regions of the base metal. To ensure that ultrasonic vibrations can effectively influence the molten pool during the welding process, it is crucial to investigate the effects of ultrasonic vibrations at various positions within the Inconel690 plate. The propagation and distribution of ultrasonic vibrations in the base metal can be characterized by distinct characteristic quantities. The difference between the pressure at a specific point in the ultrasonic field at a particular time and the static pressure at this point when the ultrasonic physical field is absent constitutes the acoustic pressure. Figure 2 shows the acoustic pressure at different positions of the plate when the simulated ultrasonic horn is applied to Inconel690 plate. Since the physical dimensions of the solid base material are fixed, when the acoustic wave is transmitted to the boundary of the base material, due to the acoustic impedance on the surface of the base material, the reflection and transmission will occur at the boundary of the base material, and the superposition of the reflected wave and the incident wave will increase the vibration at some positions of the base material surface and weaken the vibration at some positions; therefore, the propagation of ultrasonic wave on the base metal under steady state does not conform to the characteristics of spherical surface wave and presents the characteristics of high sound pressure in a specific area. The black elliptical point is the origin position of the ultrasonic vibrations, as shown in Figure 2. The acoustic pressure in front of this point exhibits a repetitive pattern of decrease and increase. Initially, it experiences an increase in negative acoustic pressure values, reaching its maximum at 90 mm. Subsequently, the acoustic pressure value rises gradually and ultimately reaches its maximum value in the forward direction again at 180 mm. Finally, the sound pressure decreases once more.

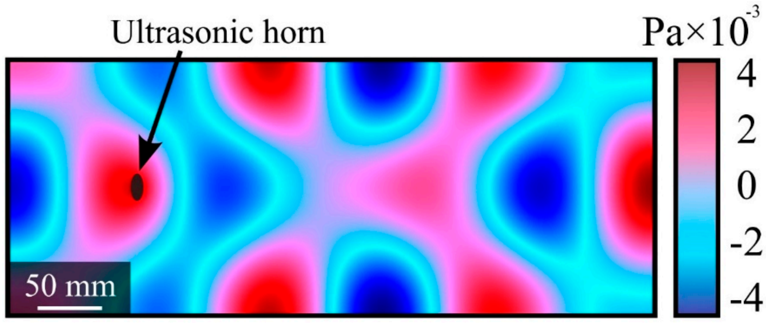

Figure 2. The simulated acoustic pressure of the Inconel690 alloy plate with the ultrasonic vibration.

Figure 3a shows the surface amplitude of the different positions on the Inconel690 plate. The surface amplitude represents the macroscopic manifestation of atomic vibrations within the plate. When the ultrasonic wave propagates through the Inconel690 plate, atoms within the medium undergo vibrational motion around their equilibrium positions in response to the acoustic disturbances. Hence, the surface amplitude can serve as a reliable indicator of the efficacy of ultrasonic vibration. And Figure 3b shows the acoustic pressure at various positions on the plate. Both amplitude distribution and acoustic pressure exhibit fluctuations with distance, showing similar patterns. The maximum amplitude occurs at distances of 90 and 180 mm from the ultrasonic horn.

Select the 6 positions (R1 (30 mm from horn), R2 (60 mm), R3 (90 mm), R4 (150 mm), R5 (180 mm), R6 (210 mm)) with high acoustic pressure and ultrasonic amplitude under steady state to further measure the stability of ultrasonic amplitude. Figure 4 shows the variation of the amplitude of the base metal surface with time when the ultrasonic horn contacts to the base metal plate. The amplitude vibration frequency at these 6 positions is 35 $\pm$ 0.05 kHz. However, the variation trend of amplitude with time at these six positions is different. The amplitudes of R1, R5, and R6 are relatively stable, and the amplitudes of the other three positions vary greatly with time, so it is difficult to achieve stable ultrasonic output during welding. The amplitude of R2 fluctuates relatively slowly over time, while the amplitude at R6 varies periodically, with each cycle approximately 1.4 ms, while the amplitude variation periods at R3 and R4 are both longer than 50 ms. To compare the amplitude fluctuations at different positions, the root mean square of the amplitude variation at different positions was plotted in Figure 5. The root mean square of amplitude variation with time of R1 and R5 are smaller than other, while the root mean square of amplitude variation at R4 is the largest. Different amplitudes have different effects on the molten pool [25]. Therefore, the position with stable amplitude can promote the stable action of ultrasonic vibration on the molten pool and improve the microstructure of welded joints.

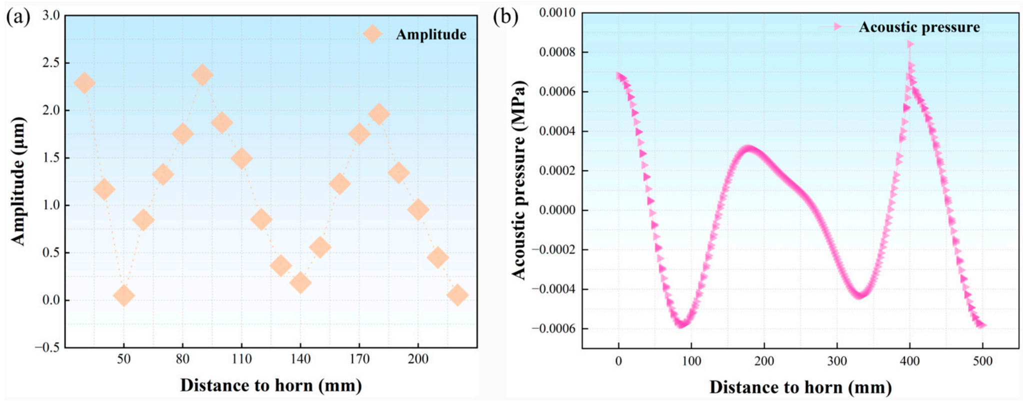

Figure 3. The amplitude and acoustic pressure of different position: (**a**) amplitude; (**b**) acoustic pressure.

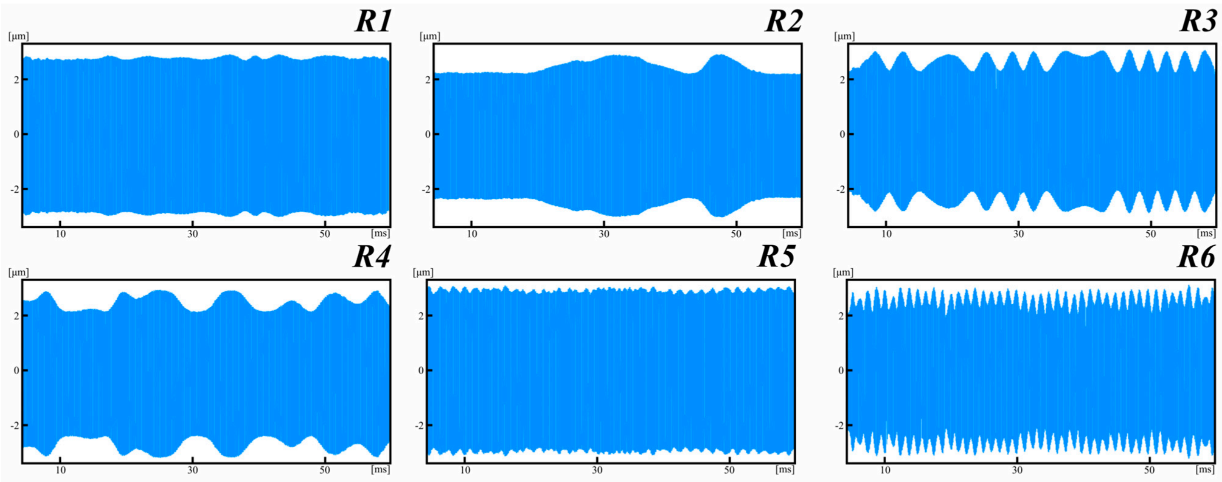

Figure 4. The amplitude variation at different positions over time.

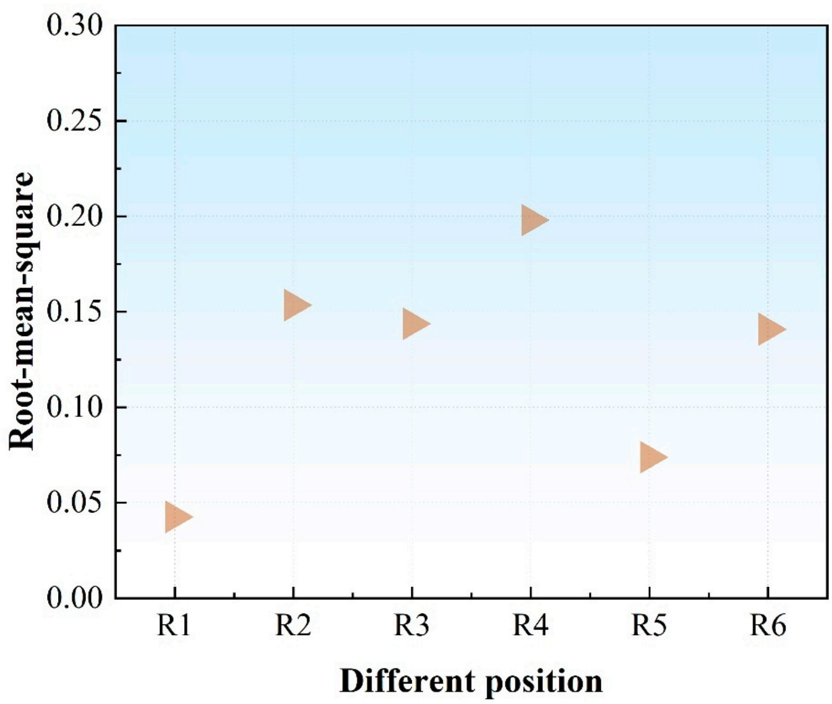

Figure 5. The root mean square of amplitude variation with time.

3.2. The Ultrasonic Effect on the Microstructure of the Weld Zone

To investigate the influence of different ultrasonic conditions on the molten pool, welding tests were conducted using Inconel690 alloy with fixed distances between the welding torch and ultrasonic horn at 30 mm (R1), 60 mm (R2), 90 mm (R3), 150 mm (R4), 180 mm (R5), and 210 mm (R6). The different welded joint samples of Inconel690 alloy were label as the WR1 (30 mm), WR2 (60 mm), WR3 (90 mm), WR4 (150 mm), WR5 (180 mm), and WR6 (210 mm) attributed the distance between the welding torch and ultrasonic horn. The microstructure revealed that nickel-based alloy welded joints consist of dendrites, with solidified grains formed by clusters of dendrites exhibiting various growth directions. The growth direction of dendrites aligns opposite the temperature gradient in a regular GTA welded joint. The microstructure of Inconel690 welded joints parallel to the welding direction provides a more precise depiction of how ultrasonic vibration influences grain growing, owing to the unique growth direction of dendrites in the Inconel690 welded joint. Figure 6 shows the microstructure of different welded joints (WR1–WR6) parallel to the welding direction. Dendrites can be observed in the microstructure of all samples. The dendrites in the weld zone of all samples grow in the opposite direction of the temperature gradient except WR5. The dendrite growth direction in WR5 is not significantly related to the temperature gradient direction and even grows perpendicular to the temperature gradient. The competitive grain growth is significant in WR1, WR2, WR4, WR5, and WR6. The dendrites in the WR3 weld zone grow vertically upwards. The microstructure reveals a significant alteration in the growth direction of dendrites with varying distances between the ultrasonic horn and welding torch.

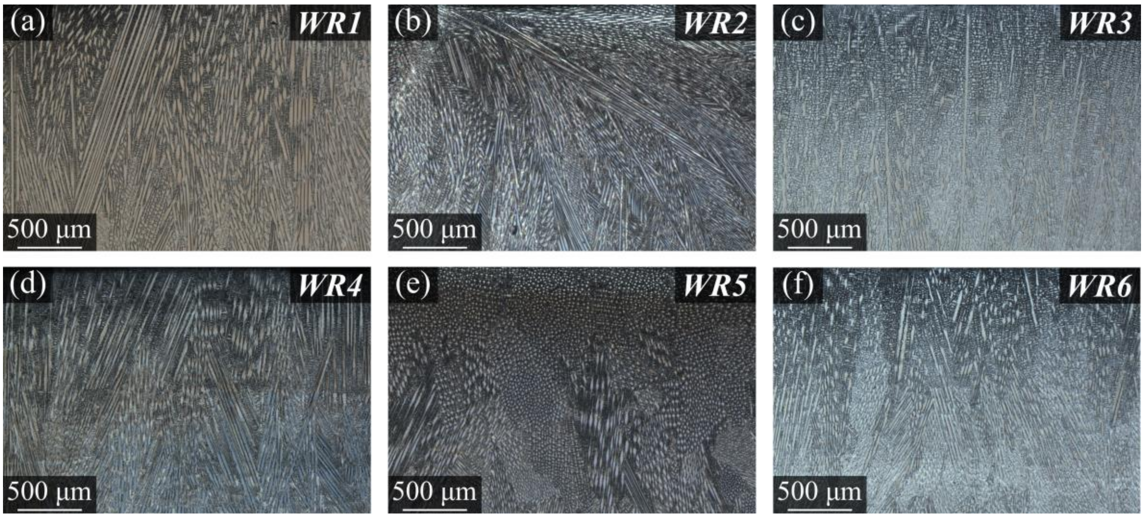

Figure 6. The OM of the weld zone: (**a**) WR1 sample; (**b**) WR2 sample; (**c**) WR3 sample; (**d**) WR4 sample; (**e**) WR5 sample; (**f**) WR6 sample.

In ultrasonic-assisted arc welding, ultrasonic vibration can change the flow of the liquid metal and the stirring effect on the molten pool under different ultrasonic conditions. The influence of ultrasonic vibrations on the flow of a molten pool is attributed to cavitation and acoustic streaming effects. When ultrasonic vibrations travel in the molten pool, due to the attenuation and reflection of ultrasonic vibrations, the acoustic pressure distribution of liquid metal is uneven, and the pressure difference leads to the flow of liquid metal. In addition, ultrasonic vibration can cause cavitations in the molten pool. The cavitations will grow and eventually collapse, accompanied by high temperature and pressure. This change in pressure and temperature around the cavities can also cause abnormal flow in the molten pool. Due to the different ultrasonic vibrations at different distances between the torch and horn, the impact on the flow of the molten pool is also different.

Figure 7 shows the competitive grain growth in the regular GTAW of Inconel690 alloy [26]. In Figure 7, grain 1 (G1) and grain 3 (G3) are the grains' growth along the temperature gradient; grain 2 (G2) is the grain whose growth direction is not parallel to the direction of temperature gradient; ΔZ is the distance between the liquid and dendrite tips; and θ is the angel between the growth direction of G3 and the temperature gradient. The grains growing closer to the direction of the temperature gradient are referred to as preferred oriented grains (G1 and G3), while G2 is considered a non-preferred oriented grain. During solidification in the molten pool, it is crucial for the dendrites of G1 and G2 to have equal growth rates in the direction of temperature gradient to ensure the upward movement of the solid–liquid interface. To maintain this equal growth rate in the axial direction of the temperature gradient, it is necessary for dendrites in the non-preferred oriented grain (G2) along the growth direction to exhibit a higher growth rate (about the dendrites growth rate of G1 multiplied by the cosine of angle θ) than those in G1. The higher growth rate requires that the tip of the dendrite be positioned further back, resulting in greater supercooling at its tip, which drives dendrite growth. Therefore, since the tip position of dendrites in non-preferred oriented grain (G2) always lags behind that of dendrites in preferred orientated grain (G1), G1 acts as a barrier preventing G2 from growing, ultimately leading to the elimination of non-preferred orientated grains during the solidification process within molten pool. Furthermore, due to a large growth space between G3 and G2, new primary dendrite arms of G3 form between G2 and G3, causing a reduction in the available growth space of non-preferred oriented grains until they are eventually eliminated.

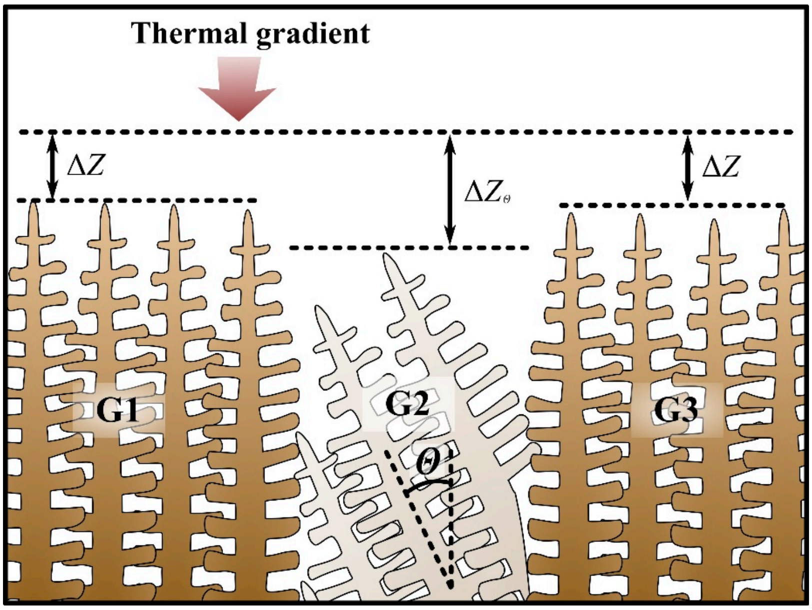

Figure 7. Schematic of the competitive grain growth during the solidification of Inconel690 alloy.

The variation in the ultrasonic effect resulting from the adjustment of the distance between the ultrasonic horn and welding torch induces alterations in the growth of non-preferred oriented grains, even leading to modifications in the preferred orientation. In the longitudinal section of the regular weld molten pool, the growth direction of the grains in the weld zone is tilted in the welding direction. When the distance between the ultrasonic horn and the torch is 30 mm, most of the non-preferred orientated grains are still hindered by the preferred orientated grains at this time, but the stirring of the molten pool caused by the ultrasonic acoustic flow effect and the cavitation effect changes the direction of the temperature gradient, which is opposite to that in the regular molten pool. This results in the presence of preferred orientated grains in the melt pool that grow in both directions. As the distance between the ultrasonic horn and the welding torch is further increased to 60 mm, the stirring effect of ultrasonic vibrations on the molten pool currently makes most of the solidified grains grow in the same direction, which indicates that ultrasonic vibrations currently do not change the direction of the temperature gradient in the molten pool and increase the temperature gradient along the direction of the weld. However, because the ultrasonic amplitude is not currently uniform, its stirring effect on the molten pool is not stable, so the growth direction of the grains in the molten pool is not completely along the temperature gradient direction. When the distance between the ultrasonic horn and the welding torch reaches 90 mm, a counter-directional flow induced by ultrasonic vibration occurs simultaneously with the motion-induced flow of the molten pool, resulting in a temperature gradient perpendicular to the welding direction and vertical growth of dendrites. When the ultrasonic horn and torch are 150 mm and 210 mm apart, the stirring effect of ultrasonic vibration on the molten pool is like that of WR1, and there are multiple dendrite growth directions in the weld. When the ultrasonic horn and torch distance is 180 mm, the ultrasonic amplitude is larger and the cavitation effect and acoustic streaming effect of ultrasonic vibration on the molten pool have a greater impact, so some of the dendrites even grow in the direction perpendicular to the longitudinal cross-section of the weld.

Ultrasonic vibration can not only change the growth direction of the dendrite but also refine the grain and improve the microstructure. In the nickel-based alloy weld, the distance between the dendrite arm spacing has a great influence on the mechanical properties of the welded joint. Therefore, by comparing the dendrite spacing in the weld zone under different distances between the ultrasonic horn and welding torch, it is possible to determine the refining effect of ultrasonic vibration on the structure and subsequently to identify the optimal distance for ultrasonic action. Figure 8 shows the measurement method of the dendrite spacing in the microstructure of a nickel-based alloy welded joint. The dendrite spacing include primary dendrite arm spacing (PDAS) and secondary dendrite arm spacing (SDAS). The PDAS is calculated as follows:

$$PDAS = \frac{L_1 + L_2 + L_3}{3}. \quad (1)$$

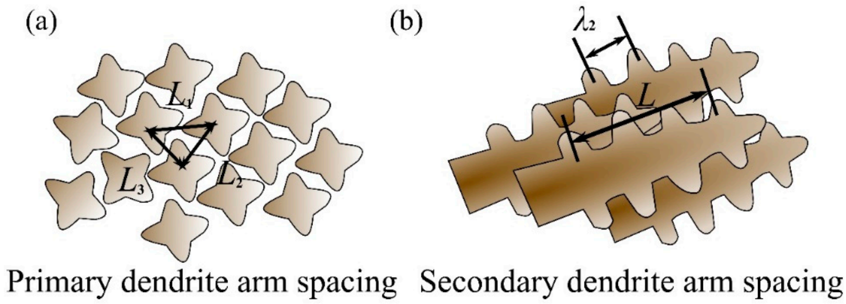

Figure 8. Schematic diagram of dendrite spacing measurement: (**a**) PDAS; (**b**) SDAS.

And the SDAS is calculated as follows:

$$SDAS = \frac{L}{n-1}. \quad (2)$$

The dendrite spacing of the welded joint was measured and is shown in Figure 9, showing fluctuation in its variation. Among the samples, WR2 and WR5 exhibited the smallest PDAS, while WR5 had the smallest SDAS. This suggests that positioning the torch at 180 mm from the ultrasonic horn yields optimal refinement effects on dendrites. Additionally, it was observed that primary and secondary dendrite arm spacings did not decrease synchronously, indicating that ultrasonic treatment has varying effects on primary and secondary dendrite arm spacings. The work of Lehmann et al. [27] proposed that the smaller the dendritic arm, the larger the flow rate. During dendritic growth, changes in the temperature field alter the conditions for nucleation to promote dendritic nucleation and the growth of primary dendrites; meanwhile, alterations in the concentration field modify the growth kinetics to achieve the refinement of primary and secondary dendrites. Figure 10 shows the hardness of the different sample. The average hardness of WR2 the WR5 are higher than others and reach 235 HV_1. The dendrites' arm spacing is more refined than in other samples. This means that there are more subgrain boundaries in both the WR2 and WR5 samples. The subgrain boundaries provide an obstacle to the movement of the dislocation, which usually results in an increase in hardness.

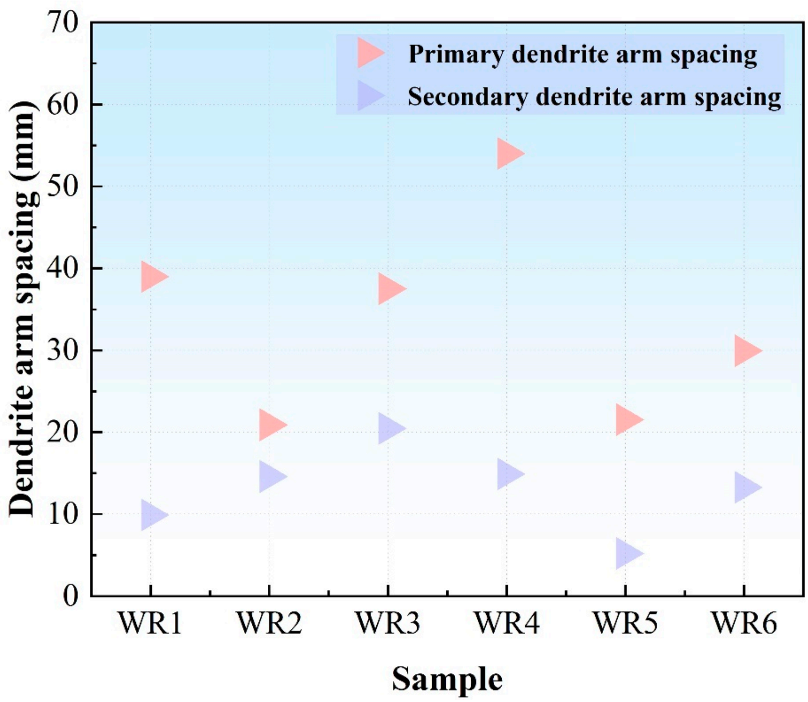

Figure 9. The dendrite spacing of different samples.

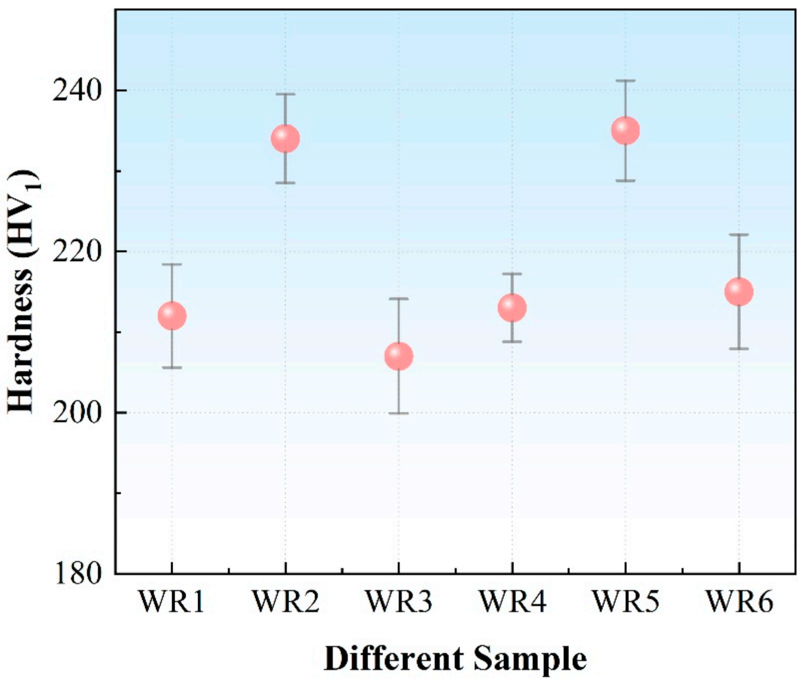

Figure 10. The hardness of different samples.

4. Conclusions

This study enhances the understanding of UA-GTAW Inconel690 alloy and presents a practical and universally applicable approach to optimizing ultrasonic-assisted welding across diverse alloys. In this study, the acoustic pressures were simulated and the amplitudes were measured at different distances on the Inconel690 plate. The microstructure of the welded joints at different distances between the ultrasonic horn and welding torch was studied. The conclusions of this work are as follows.

(1) The distribution of acoustic pressure and ultrasonic amplitude on Incoenl690 alloy plates does not conform to the spherical wave pattern. The ultrasonic amplitude does not necessarily increase as the distance to the ultrasonic horn decreases; instead, it reaches its maximum value at distances of 90 mm and 180 mm from the horn.

(2) Ultrasonic vibration has different effects on the growth direction of dendrites at different positions. With the increase in distance between welding torch and ultrasonic horn, the influence of ultrasonic vibration on the convection of the molten pool changes, which then affects the growth direction of dendrites in the weld. At 90 mm, it causes the dendrites to grow vertically; and at 180 mm, it causes the dendrites to grow horizontally.

(3) The synergistic refinement effect of primary and secondary dendrites is maximized when the distance between the ultrasonic horn and the welding torch is precisely 60 and 180 mm.

(4) The dendrite refinement caused by ultrasonic vibration will increase the hardness of the weld zone. The ultrasonic influences on weld hardness are affected by the distance between the ultrasonic horn and welding torch. The WR2 and WR5 samples with the smallest dendrites have the highest hardness, which can reach 235 HV_1.

Author Contributions: Conceptualization, S.L. and Y.X.; methodology, B.D.; software, B.D.; validation, X.C. and S.L.; formal analysis, Y.X.; investigation, Y.X.; resources, S.L.; data curation, Y.X.; writing—original draft preparation, Y.X.; writing—review and editing, S.L.; visualization, Y.X.; supervision, X.C.; project administration, S.L.; funding acquisition, S.L. All authors have read and agreed to the published version of the manuscript.

Funding: This research was funded by the National Natural Science Foundation of China grant number 52175296.

Data Availability Statement: Data are not available since the data in this study will be used in our current research works.

Conflicts of Interest: The authors declare no conflict of interest.

References

1. Zhang, D.; Zhang, H.-C.; Li, Z.-E.; Wang, Q.; Sun, W.-B. Investigation on Entropy Generation and Flow Characteristics of 7-Pin Sodium Cooled Wrapped-Wire Fuel Bundle. *Int. Commun. Heat Mass Transf.* **2022**, *137*, 106280. [CrossRef]
2. Zhang, D.; Zhang, H.; Wang, Q.; Sun, W. Effect of Heat Flux Distribution on Entropy Generation and Irreversibility of Lead-Bismuth Eutectic (LBE) Forced Convective Heat Transfer. *J. Therm. Sci.* **2023**, *32*, 223–236. [CrossRef]
3. Park, N.K.; Kim, J.J.; Chai, Y.S.; Lee, H.S. Microstructural Evolution of Inconel 690 Alloy for Steam Generator Tubes. *Key Eng. Mater.* **2007**, *353–358*, 1609–1613. [CrossRef]
4. Li, H.; Xia, S.; Zhou, B.; Chen, W.; Hu, C. The Dependence of Carbide Morphology on Grain Boundary Character in the Highly Twinned Alloy 690. *J. Nucl. Mater.* **2010**, *399*, 108–113. [CrossRef]
5. Li, Y.; Wang, J.; Han, E.-H.; Wu, W.; Hänninen, H. Multi-Scale Study of Ductility-Dip Cracking in Nickel-Based Alloy Dissimilar Metal Weld. *J. Mater. Sci. Technol.* **2019**, *35*, 545–559. [CrossRef]
6. Dubberstein, T.; Heller, H.-P.; Fabrichnaya, O.; Aneziris, C.G.; Volkova, O. Determination of Viscosity for Liquid Fe–Cr–Mn–Ni Alloys. *Steel Res. Int.* **2016**, *87*, 1024–1029. [CrossRef]
7. Yan, Z.; Hu, Q.; Jiang, F.; Lin, S.; Li, R.; Chen, S. Mechanism and Technology Evaluation of a Novel Alternating-Arc-Based Directed Energy Deposition Method through Polarity-Switching Self-Adaptive Shunt. *Addit. Manuf.* **2023**, *67*, 103504. [CrossRef]
8. Zhu, Z.Y.; Liu, Y.L.; Gou, G.Q.; Gao, W.; Chen, J. Effect of Heat Input on Interfacial Characterization of the Butter Joint of Hot-Rolling CP-Ti/Q235 Bimetallic Sheets by Laser + CMT. *Sci. Rep.* **2021**, *11*, 10020. [CrossRef]
9. Zhang, Z.; Han, Y.; Lu, X.; Zhang, T.; Bai, Y.; Ma, Q. Effects of N_2 Content in Shielding Gas on Microstructure and Toughness of Cold Metal Transfer and Pulse Hybrid Welded Joint for Duplex Stainless Steel. *Mater. Sci. Eng. A* **2023**, *872*, 144936. [CrossRef]

10. Wang, J.; Sun, Q.; Teng, J.; Jin, P.; Zhang, T.; Feng, J. Enhanced Arc-Acoustic Interaction by Stepped-Plate Radiator in Ultrasonic Wave-Assisted GTAW. *J. Mater. Process. Technol.* **2018**, *262*, 19–31. [CrossRef]
11. Wang, L.; Cong, B.; Liu, F.; Qi, B.; Yang, M.; Li, W. Weld formation characteristics in hybrid ultra-high frequency pulse variable polarity GTAW of 2219-T87 high strength aluminum alloy. *Han Jie Xue Bao* **2013**, *34*, 61–64.
12. Wang, Y.; Cong, B.; Qi, B.; Yang, M.; Lin, S. Process Characteristics and Properties of AA2219 Aluminum Alloy Welded by Double Pulsed VPTIG Welding. *J. Mater. Process. Technol.* **2019**, *266*, 255–263. [CrossRef]
13. Aoki, S.; Kurita, K.; Koshimizu, S. Reduction of Residual Stress on Welded Joint Using Two Ultrasonic Vibrations. *J. Jpn. Soc. Technol. Plast.* **2017**, *58*, 47–52. [CrossRef]
14. Watanabe, T.; Shiroki, M.; Yanagisawa, A.; Sasaki, T. Improvement of Mechanical Properties of Ferritic Stainless Steel Weld Metal by Ultrasonic Vibration. *J. Mater. Process. Technol.* **2010**, *210*, 1646–1651. [CrossRef]
15. Fattahi, M.; Ghaheri, A.; Arabian, N.; Amirkhanlu, F.; Moayedi, H. Applying the Ultrasonic Vibration during TIG Welding as a Promising Approach for the Development of Nanoparticle Dispersion Strengthened Aluminum Weldments. *J. Mater. Process. Technol.* **2020**, *282*, 116672. [CrossRef]
16. Tian, Y.; Shen, J.; Hu, S.; Wang, Z.; Gou, J. Effects of Ultrasonic Vibration in the CMT Process on Welded Joints of Al Alloy. *J. Mater. Process. Technol.* **2018**, *259*, 282–291. [CrossRef]
17. Koli, Y.; Yuvaraj, N.; Aravindan, S. Vipin Enhancement of Mechanical Properties of 6061/6082 Dissimilar Aluminium Alloys Through Ultrasonic-Assisted Cold Metal Transfer Welding. *Arab. J. Sci. Eng.* **2021**, *46*, 12089–12104. [CrossRef]
18. Wang, Y.; Liu, W.; Wang, D.; Yu, C.; Xu, J.; Lu, H.; Chen, J. Simultaneously Enhanced Strength and Ductility of TIG Welds in Inconel 718 Super-Alloy via Ultrasonic Pulse Current. *Mater. Sci. Eng. A* **2021**, *807*, 140894. [CrossRef]
19. Wang, Y.; Wang, H.; Chen, J.; Zheng, Y.; Li, C.; Liu, T.; Hao, L.; Kejin, Z. Achieving Polycrystalline Transformation and Microstructural Segregation Reduction of Nickel-Based Single Crystal Super-Alloys by Ultrasonic Pulse Arc Welding. *J. Mater. Res. Technol.* **2023**, *24*, 2200–2212. [CrossRef]
20. Wang, Y.; Yu, C.; Lu, H.; Chen, J. Research Status and Future Perspectives on Ultrasonic Arc Welding Technique. *J. Manuf. Process.* **2020**, *58*, 936–954. [CrossRef]
21. Chen, Z.-J.; Zhang, S.-Y.; Zheng, K. Nonlinear vibration in metal plate excited by high-power ultrasonic pulses. *Acta Phys. Sin.* **2010**, *59*, 4071–4083. [CrossRef]
22. Chen, Z.; Zhang, S.; Zheng, K.; Zhang, T.; Zhou, F. Subharmonic Vibrations in Plates Excited by High-Intensive Ultrasonic Pulses. In Proceedings of the 2008 IEEE Ultrasonics Symposium, Beijing, China, 2–5 November 2008; pp. 1804–1807.
23. Ranjan, R.; Jha, S.K. Optimization of Welding Parameters and Microstructure Analysis of Low Frequency Vibration Assisted SMAW Butt Welded Joints. *Int. J. Interact. Des. Manuf.* **2023**, 1–21. [CrossRef]
24. Li, Y.; Tian, S.; Wu, C.; Tanaka, M. Experimental Sensing of Molten Flow Velocity, Weld Pool and Keyhole Geometries in Ultrasonic-Assisted Plasma Arc Welding. *J. Manuf. Process.* **2021**, *64*, 1412–1419. [CrossRef]
25. Wang, J.; Lu, C.; Xiao, C.; Cheng, J.; Ren, R.; Xiong, X. Heat Distribution Simulation and Effects of Ultrasonic Welding Amplitude on Carbon Fiber/Polyetherimide Composite Joint Properties. *Mater. Lett.* **2023**, *340*, 134148. [CrossRef]
26. Hughes, T.; Robinson, A.J.; McFadden, S. Competitive Growth during Directional Solidification Experiments of ⟨1 1 1⟩ Dendrites. *J. Cryst. Growth* **2022**, *599*, 126893. [CrossRef]
27. Lehmann, P.; Moreau, R.; Camel, D.; Bolcato, R. A Simple Analysis of the Effect of Convection on the Structure of the Mushy Zone in the Case of Horizontal Bridgman Solidification. Comparison with Experimental Results. *J. Cryst. Growth* **1998**, *183*, 690–704. [CrossRef]